Weierstraß-Institut

für Angewandte Analysis und Stochastik

Leibniz-Institut im Forschungsverbund Berlin e. V.

A comparative study of a direct discretization and an operator-splitting solver for population balance systems

Felix Anker[1], Sashikumaar Ganesan[2] , Volker John[1,3] , Ellen Schmeyer[1]

submitted: October 10, 2014

[1] Weierstrass Institute
Mohrenstr. 39
10117 Berlin
Germany
email: Felix.Anker@wias-berlin.de
Volker.John@wias-berlin.de
Ellen.Schmeyer@wias-berlin.de

[2] Indian Institute of Science
Supercomputer Education and Research Centre
Bangalore - 560012
India
email: sashi@serc.iisc.in

[3] Free University of Berlin
Department of Mathematics and Computer Science
Arnimallee 6
14195 Berlin
Germany

No. 2022

Berlin 2014

Abstract

A direct discretization approach and an operator-splitting scheme are applied for the numerical simulation of a population balance system which models the synthesis of urea with a uni-variate population. The problem is formulated in axisymmetric form and the setup is chosen such that a steady state is reached. Both solvers are assessed with respect to the accuracy of the results, where experimental data are used for comparison, and the efficiency of the simulations. Depending on the goal of simulations, to track the evolution of the process accurately or to reach the steady state fast, recommendations for the choice of the solver are given.

1 Introduction

Population balance systems (PBSs) model particulate flows where not the behavior of the individual particles is of interest but the behavior of the particles in the mean. To this end, the particle population is described with a particle size distribution (PSD) and an equation for the PSD is derived whose terms model, e.g., transport, nucleation, growth, and aggregation of particles. Together with equations for the energy or mass balance and an equation which describes the flow field, the behavior of the particulate flow is modeled with a so-called PBS.

A major challenge for the numerical simulation of PBSs arises from the fact that the PSD not only depends on time and space, like, e.g., the flow field and the temperature, but also on properties of the particles, the so-called internal coordinates. After having applied a temporal discretization to the PBS, the equation for the PSD is given in a domain whose dimension is the sum of the spatial dimension and the number of internal coordinates.

One can find in the literature different proposals for dealing with the high dimensionality of the equation for the PSD. A direct discretization of the high-dimensional equation was studied, e.g., in [4,17,19,20]. This approach is motivated by a potentially good accuracy of the computed solution, since no simplifications to the original problem were applied. However, the numerical solution of an equation in a higher-dimensional domain is rather expensive. Motivated by performing more efficient simulations, other approaches were proposed. Moment-based methods, like the quadrature method of moments (QMOM) or the direct QMOM (DQMOM) [23,24] replace the equation for the PSD by a system of equations for the first moment, with respect to the internal coordinates, of the PSD. These methods are quite popular in the engineering community. But the original PBS is modified quite strongly and the reconstruction of the PSD from the first moments is a severely ill-posed problem [15]. Another approach motivated by efficiency, which does not change the original PBS, is the operator-splitting scheme proposed in [6]. This scheme splits the computation of the solution into subproblems with respect to the spatial and to the internal coordinates [6,10]. To the best of our knowledge, systematic numerical comparisons of these different schemes have not been performed in the literature so far.

The goal of this paper consists in performing the first step in the systematic assessment of different solvers for PBSs. In this step, a direct discretization and an operator-splitting scheme are studied. This choice is motivated by our rich experience with these methods.

For an assessment of numerical methods, one needs a problem where some ref-

erence values of the solution are known. To this end, a model of urea synthesis from [14], with a uni-variate population, will be used where some experimental data from [3] are available. This model will be considered in a comparable simple situation: the flow domain is a cylindrical pipe, the flow fields are stationary, the velocity field is given by a Hagen–Poiseuille profile, and the setup is such that the solution, in cylindrical coordinates, can be assumed to be independent of the angle. Since the velocity field is known, there is no need to solve the Navier–Stokes equations. Thus, the computing times of the different numerical methods for solving the equation for the PSD will constitute a large part of the overall computing times of the simulations. From the independence of the angle, it follows that the PBS can be written in axisymmetric form which reduces the spatial dimension from three to two.

The paper is organized as follows. Section 2 presents the population balance model for the urea synthesis. The solvers for the PBS are describe in Section 3. Section 4 presents the numerical studies and an outlook will be given in Section 5.

2 The Population Balance Model of the Urea Synthesis

This section presents the population balance system which models the urea synthesis. It is in principal the same model as considered in [14]. Only, the flow domain has a different form, hence also the flow field, such that a 3D-axisymmetric form of this model can be used in the numerical simulations. It will be explained in Section 4 that the different flow field will also change the impact of growth and aggregation on the urea population compared with [14].

The model for the considered urea population consists of a system of equations describing the energy balance, the mass balance of the dissolved urea, and the behavior of the PSD.

For the flow field $\boldsymbol{u}$ [m/s] in the cylindrical domain $\Omega \subset \mathbb{R}^3$ a Hagen–Poiseuille profile is assumed. The boundary of Ω is composed of the inlet Γ_{in}, the outlet Γ_{out}, and the wall Γ_{wall}.

Let $m_{\text{mol}} = 60.06 \cdot 10^{-3}$ [kg/mol] be the molar mass of urea, then the saturation concentration of the dissolved urea is given by

$$c_{\text{sat}}(T) = \frac{35.364 + 1.305(T - 273.15)}{m_{\text{mol}}} \ [\text{mol/m}^3], \tag{1}$$

where T is the temperature in the system. Further, the growth rate of the

3

urea particles is modeled by

$$G(c, T) = \begin{cases} k_g \left(\dfrac{c - c_{\text{sat}}(T)}{c_{\text{sat}}(T)} \right)^g, & \text{if } c > c_{\text{sat}}(T), \\ 0, & \text{else,} \end{cases} \quad [\text{m}/\text{s}], \qquad (2)$$

with the growth rate constant $k_g = 10^{-7}$ [m/s] and the growth rate power $g = 0.5$ [·]. Here, c [mol/m³] is the mass of the solute, and its evolution is described by

$$\frac{\partial c}{\partial t} - D\Delta c + \boldsymbol{u} \cdot \nabla c + \frac{H_\ell}{m_{\text{mol}}} = \frac{f_\ell}{m_{\text{mol}}} \quad \text{in } (0, t_e) \times \Omega, \qquad (3)$$

where

$$H_\ell = 3\rho^d k_V G(c, T) \int_{\ell_{\min}}^{\ell_{\max}} \ell^2 f \, d\ell, \quad \text{and} \quad f_\ell = -\rho^d k_V \ell_{\min}^3 B_{\text{nuc}}.$$

In this equation, $D = 1.35 \cdot 10^{-9}$ [m²/s] is the diffusion coefficient of urea in ethanol, $\rho^d = 1323$ [kg/m³] is the density of urea (dispersed phase), $k_V = \pi/6$ [·] is the scaling factor from diameters to volume (where it is assumed that all particles are of spherical shape) and t_e [s] is the final time for the simulations. The nucleation rate B_{nuc} is defined by

$$B_{\text{nuc}} = \alpha_{\text{nuc}} \exp \left(\frac{-\beta_{\text{nuc}}}{\ln^2(c/c_{\text{sat}}(T))} \right),$$

where $\alpha_{\text{nuc}} = 1 \cdot 10^8$ is the nucleation constant and $\beta_{\text{nuc}} = 1.66667 \cdot 10^{-4}$ is a model constant. The PSD is denoted by f [1/m⁴] and the diameter of the particles is ℓ [m], where $\ell_{\min}$ is the smallest diameter (nuclei size) and $\ell_{\max}$ is an upper bound for the largest diameter. The last term on the left-hand side of (3) describes the decrease of dissolved urea due to the growth of particles and the term on the right-hand side models the consumption of dissolved urea due to the nucleation of particles. Equation (3) has to be equipped with initial and boundary conditions. The boundary condition is given by

$$\begin{cases} c(t, \boldsymbol{x}) = c_{\text{sat}}(T_{\text{in}}), \ \boldsymbol{x} \in \Gamma_{\text{in}}, \\ D\dfrac{\partial c}{\partial \boldsymbol{n}_\Gamma} = 0, & \boldsymbol{x} \in \Gamma_{\text{out}} \cup \Gamma_{\text{wall}}, \end{cases} \qquad (4)$$

where $\boldsymbol{n}_\Gamma$ is the outward pointing unit normal on Γ and T_{in} is the temperature at the inlet, see (6) below. In addition, an initial condition is needed for closing equation (3). Since such a condition is not known from the experiments, the inlet concentration value is used as the initial value, that is

$$c(0, \boldsymbol{x}) = c_{\text{sat}}(T_{\text{in}}) \quad \boldsymbol{x} \in \Omega.$$

4

The model for the energy balance is of the same type as the model of the mass balance

$$\rho c_p \left(\frac{\partial T}{\partial t} + \boldsymbol{u} \cdot \nabla T \right) - \lambda \Delta T + \delta h_{\text{cryst}} H_\ell = \delta h_{\text{cryst}} f_\ell \quad \text{in } (0, t_e) \times \Omega. \tag{5}$$

In this energy equation, $\rho = 789$ [kg/m³] is the density of ethanol at 298 K, $c_p = 2441.3$ [J/(kg K)] is the specific heat capacity of ethanol, $\lambda = 0.167$ [J/(K m s)] is its thermal conductivity, and $\delta h_{\text{cryst}} = 2.1645 \cdot 10^5$ [J/kg] is the heat of solution (enthalpy change of solution). The term on the right-hand side of (5) describes the decrease of temperature resulting from the nucleation of particles and the last term on the left-hand side the decrease of the temperature due to the consumption of energy by the growth of the particles. The know boundary conditions from the experiments are

$$\begin{cases} T(t, \boldsymbol{x}) = T_{\text{in}}, & \boldsymbol{x} \in \Gamma_{\text{in}}, \\ \lambda \dfrac{\partial T}{\partial \boldsymbol{n}_\Gamma} = 0, & \boldsymbol{x} \in \Gamma_{\text{out}}, \\ T(t, \boldsymbol{x}) = T_{\text{wall}}, & \boldsymbol{x} \in \Gamma_{\text{wall}}, \end{cases} \tag{6}$$

with $T_{\text{in}} = 301.15$ [K] and $T_{\text{wall}} = 291.15$ [K]. Hence, the suspension is cooled at the wall. The initial condition was used in the same way as for the solute mass balance, that is,

$$T(0, \boldsymbol{x}) = T_{\text{in}} \quad \boldsymbol{x} \in \Omega.$$

Finally, the model for the behavior of the PSD is presented. It is assumed that the particles are of spherical shape such that they can be modeled with their diameter. Then, the equation for the PSD is given by

$$\frac{\partial f}{\partial t} + G(c, T) \frac{\partial f}{\partial \ell} + \boldsymbol{u} \cdot \nabla f = A_+ + A_-, \tag{7}$$

where A_+ is the source of the aggregation model and A_- is its sink. The presentation of the model for the aggregation, and also its implementation, is simpler if the volume of the particles is used instead of the diameter. With respect to the volume $V = k_V \ell^3$ the PSD is given by

$$f_V(V) = f_V(k_V \ell^3) = \frac{f(\ell)}{k_V} \frac{1}{3L^2} \quad [1/\text{m}^6]. \tag{8}$$

The source term describes the amount of particles of volume V which are created by the aggregation of two particles with volume V' and $V - V'$, $V' \in (0, V)$

$$A_{+,V} = \frac{1}{2} \int_0^V \kappa_{\text{agg}}(V - V', V') f_V(V - V') f_V(V') \, dV'. \tag{9}$$

The sink term describes the amount of particles of volume V that vanish because they are consumed by aggregations with other particles of volume $V' \in (0, V_{\mathrm{max}})$

$$
\begin{aligned}
A_{-,V} &= -\int_0^{V_{\mathrm{max}}} \kappa_{\mathrm{agg}}(V,V') f_V(V) f_V(V') \, dV' \\
&= -f_V(V) \int_0^{V_{\mathrm{max}}} \kappa_{\mathrm{agg}}(V,V') f_V(V') \, dV'.
\end{aligned}
\tag{10}
$$

Thus, the change of particles of volume V due to the aggregation is given by $A_{+,V} + A_{-,V}$. The change with respect to the diameter is then obtained by

$$
A_+ + A_- = 3k_V (A_{+,V} + A_{-,V}) \, \ell^2,
$$

compare (8). The aggregation kernel is the product of two factors

$$
\kappa_{\mathrm{agg}}(V,V') = p_{\mathrm{col}}(V,V') p_{\mathrm{eff}}(V,V') \; [\mathrm{m}^3/\mathrm{s}].
$$

Here, p_{col} gives the probability of the collision of particles with volume V and V'. The efficiency of the collisions, i.e., the amount of collisions which actually lead to aggregations, is described by p_{eff}. Due to the lack of models, this factor is chosen to be constant. This constant can be included into scaling factors for the individual terms of the following kernel

$$
\begin{aligned}
\kappa_{\mathrm{agg}}(V,V') = & \, C_{\mathrm{br}} \frac{2k_B T}{3\mu} \left(\sqrt[3]{V} + \sqrt[3]{V'} \right) \left(\frac{1}{\sqrt[3]{V}} + \frac{1}{\sqrt[3]{V'}} \right) \\
& + \frac{C_{\mathrm{sh}}}{k_V} \sqrt{2\nabla \boldsymbol{u} : \nabla \boldsymbol{u}} \left(\sqrt[3]{V} + \sqrt[3]{V'} \right)^3 \; [\mathrm{m}^3/\mathrm{s}],
\end{aligned}
\tag{11}
$$

where $k_B = 1,3806504 \, 10^{-23} \; [\mathrm{J/K}]$ is the Boltzmann constant, $\mu = 1.074 \; [\mathrm{kg/(m\ s)}]$ is the dynamic viscosity of ethanol at 298 K, and $C_{\mathrm{br}}, C_{\mathrm{sh}}$ are constants that have to be calibrated on the basis of the experimental data. The first term in (11) is Brownian-motion-generated. It is important for small particles since in this case the last factor becomes large. The second term is shear-induced [26] and it becomes important if both particles are large.

The initial condition for the PSD is given by

$$
f(0, \boldsymbol{x}, \ell) = 0 \quad \text{in } \Omega \times (\ell_{\mathrm{min}}, \ell_{\mathrm{max}}),
$$

i.e., there are no particles in the flow domain. Boundary conditions are necessary at the closure of the inflow boundaries

$$
f(t, \boldsymbol{x}, \ell) = \begin{cases} f_{\mathrm{in}}(t, \boldsymbol{x}, \ell), \; \boldsymbol{x} \in \Gamma_{\mathrm{in}} \\ \dfrac{B_{\mathrm{nuc}}}{G(c,T)}, & \text{at } \ell = \ell_{\mathrm{min}}, \text{ if } G(c,T) > 0. \end{cases}
$$

The PSD at Γ_{in} is given by experimental data, see [14].

For performing numerical simulations, the model has to be transferred into a dimensionless form. Let $X_\infty = 0.01$ m and $\ell_\infty = \ell_{\max} = 5 \cdot 10^{-3}$ m, be the reference lengths of the spatial domain and the diameter of the particles, respectively. Further, let $U_\infty = 0.01$ m/s, $c_\infty = 10^3$ mol/m³, $T_\infty = 1$ K and $f_\infty = 10^{13}$ 1/m⁴ be the reference values of the velocity, concentration, temperature and PSD, respectively. Then, dimensionless quantities are defined by

$$
\bar{\boldsymbol{x}} = \frac{\boldsymbol{x}}{X_\infty}, \quad \bar{\ell} = \frac{\ell}{\ell_\infty}, \quad \bar{t} = \frac{tU_\infty}{X_\infty}, \quad \bar{\ell}_{\min} = \frac{\ell_{\min}}{\ell_\infty}, \quad \bar{\ell}_{\max} = \frac{\ell_{\max}}{\ell_\infty},
$$
$$
\bar{T} = \frac{T}{T_\infty}, \quad \bar{c} = \frac{c}{c_\infty}, \quad \bar{f} = \frac{f}{f_\infty}, \quad Pe_c = \frac{X_\infty U_\infty}{D_c}, \quad Pe_T = \frac{X_\infty U_\infty c_p \rho}{\lambda},
$$

with $\ell_{\min} = 2.5 \cdot 10^{-6}$ m. Using these dimensionless variables and numbers, and omitting the bar afterwards, the dimensionless form of the multi-dimensional population balance system becomes

$$
\frac{\partial c}{\partial t} - \frac{1}{Pe_c}\Delta c + \boldsymbol{u} \cdot \nabla c + H_{\mathrm{gr}}^c = f_\ell^c \qquad \text{in } (0, t_e) \times \Omega,
$$
$$
\frac{\partial T}{\partial t} - \frac{1}{Pe_T}\Delta T + \boldsymbol{u} \cdot \nabla T + H_{\mathrm{gr}}^T = f_\ell^T \qquad \text{in } (0, t_e) \times \Omega,
$$
$$
\frac{\partial f}{\partial t} + \boldsymbol{u} \cdot \nabla f + \frac{X_\infty}{U_\infty \ell_\infty}G\frac{\partial f}{\partial \ell} = \frac{X_\infty}{U_\infty f_\infty}\left(A_+ + A_-\right) \quad \text{in } (0, t_e) \times \Omega \times \Omega_\ell.
$$

$$(12)$$

Here, Ω_ℓ denotes the scaled domain of the internal domain $(\ell_{\min}, \ell_{\max})$ and the dimensionless terms are

$$
H_{\mathrm{gr}}^c = \frac{H_\ell}{m_{\mathrm{mol}}} = \frac{X_\infty \ell_\infty^3 f_\infty}{U_\infty c_\infty} \cdot \frac{3\rho^d k_V}{m_{\mathrm{mol}}}G(c, T)\int_{\Omega_\ell}\ell^2 f\, d\ell,
$$
$$
f_\ell^c = -\frac{X_\infty \ell_\infty^3}{U_\infty c_\infty} \cdot \frac{\rho^d k_V \ell_{\min}^3 B_{\mathrm{nuc}}}{m_{\mathrm{mol}}},
$$
$$
H_{\mathrm{gr}}^T = \delta h_{\mathrm{cryst}} H_\ell = \frac{X_\infty \ell_\infty^3 f_\infty}{U_\infty T_\infty} \cdot \frac{3\rho^d k_V \delta h_{\mathrm{cryst}}}{c_p \rho}G(c, T)\int_{\Omega_\ell}\ell^2 f\, d\ell,
$$
$$
f_\ell^T = -\frac{X_\infty \ell_\infty^3}{U_\infty T_\infty} \cdot \frac{\delta h_{\mathrm{cryst}}\rho^d k_V \ell_{\min}^3 B_{\mathrm{nuc}}}{c_p \rho}.
$$

The dimensionless initial and boundary conditions become

$$f(t, \boldsymbol{x}, \ell_{\min}) = \begin{cases} \dfrac{B_{\mathrm{nuc}}}{G f_{\infty}}, & \text{if } G > 0. \\ 0, & \text{else.} \end{cases}$$

$$c = 1.1972, \quad T = 301.15, \quad f = \frac{f_{\mathrm{in}}}{f_{\infty}} \quad \text{on } \Gamma_{\mathrm{in}},$$

$$\frac{\partial c}{\partial \boldsymbol{n}_{\Gamma}} = 0, \quad T = \frac{T_{\mathrm{wall}}}{T_{\infty}}, \quad \text{on } \Gamma_{\mathrm{wall}},$$

$$\frac{\partial c}{\partial \boldsymbol{n}_{\Gamma}} = 0, \quad \frac{\partial T}{\partial \boldsymbol{n}_{\Gamma}} = 0, \quad \text{on } \Gamma_{\mathrm{out}}.$$

3   The Studied Solvers of the Population Balance System

In this section, the two solvers that will be compared in the simulations are presented. Then the transform of the dimensionless system (12) into an axisymmetric form is described. Finally, the algorithm for computing the aggregation term is briefly discussed.

Let $0 = t^0 < t^1 < \cdots < t^N = t_e$ be a decomposition of the considered time interval $[0, t_e]$ and let $\tau = t^n - t^{n-1}$, $1 \leq n \leq N$, denote the uniform time steps. For brevity, the superscript n is used to denote a variable at time t^n, e.g., $c^n(\boldsymbol{x}) := c(t^n, \boldsymbol{x})$.

3.1   The Direct Discretization

A detailed description of the general approach can be found in [14]. Consider the time t^n. In the first step of the direct discretization, the concentration and the energy equation of (12) are solved as a coupled system. In this system, the particle size distribution is used explicitly, i.e., f^{n-1} is used in H_{gr}^c and H_{gr}^T. The system is still coupled, since the growth rate depends on both the concentration and the temperature. It is solved iteratively, using a fixed point iteration. Since in the considered processes of urea synthesis there are usually only small changes from one time step to the next one, it turned out that generally one iteration per time step was sufficient to satisfy the stopping criterion with respect to the smallness of the residual.

In the second step, the equation for the particle size distribution in (12) is discretized on $\Omega \times \Omega_{\ell}$. Thus, a discretization in a high-dimensional (spatial dimension + number of internal coordinates) domain is applied. For computing $G, A_+,$ and A_-, the concentration and the temperature obtained in the first

step are used.

In both steps, one can apply different discretizations. Extensive numerical studies were performed in [4,17,19,20] to assess a number of possible discretizations. For the simulations presented in this paper, those discretizations were used which performed best in these studies. Thus, for discretizing the first two equations in (12), a Crank–Nicolson time integrator in combination with a linear FEM-FCT scheme [22] was applied. The equation for the particle size distribution was discretized with an explicit third order total variation diminishing (TVD) Runge–Kutta scheme in time and an essentially non-oscillatory (ENO) finite difference method in space. For the sake of brevity, it is referred to [4,18] for detailed descriptions of these schemes.

3.2 The Operator-Splitting Scheme

The splitting scheme for the PBS has first been proposed in [6], and two practical finite element algorithms have been presented in [9,10]. Later, this splitting scheme has been studies for different discretization and applications, see for example [1,2,7,11,21]. One of the main advantages, besides the splitting of a high-dimensional equation into a system of low-dimensional equations, is that the operator-splitting scheme allows to use different discretizations for each equation in the low-dimensional system. Here, the operator-splitting scheme is presented briefly, it is referred to [6,11] for more details.

Consider the time interval $(t^{n-1}, t^n]$, and the solution of (12) at t^n has to be computed from the given or computed solution at t^{n-1}. In the splitting scheme, the numerical solution of the coupled multi-dimensional system (12) is obtained in two steps. A splitting is applied to the concentration and the energy equation in (12) to decouple each other, whereas the PSD equation in (12) is split into two equations, one in the spatial space (X-direction) and another in the internal space (L-direction), respectively. After applying the splitting scheme to (12), it reads:

X-direction (Step 1):
For given $\hat{c}^{n-1} = c^{n-1}(\boldsymbol{x})$, $\hat{T}^{n-1} = T^{n-1}(\boldsymbol{x})$, and $\hat{f}^{n-1} = f^{n-1}(\boldsymbol{x}, \ell)$, find $\hat{c}$, $\hat{T}$

and $\hat{f}$ in such that for all $\ell \in \Omega_\ell$

$$\frac{\partial \hat{c}}{\partial t} + \boldsymbol{u} \cdot \nabla \hat{c} = \frac{1}{Pe_c} \Delta \hat{c} \quad \text{in } (t^{n-1}, t^n) \times \Omega,$$

$$\frac{\partial \hat{T}}{\partial t} + \boldsymbol{u} \cdot \nabla \hat{T} = \frac{1}{Pe_T} \Delta \hat{T} \quad \text{in } (t^{n-1}, t^n) \times \Omega, \qquad (13)$$

$$\frac{\partial \hat{f}}{\partial t} + \boldsymbol{u} \cdot \nabla \hat{f} = 0 \quad \text{in } (t^{n-1}, t^n) \times \Omega,$$

by considering the internal space variable ℓ as a parameter.

L-direction (Step 2)
For given $\tilde{c}^{n-1} = \hat{c}$, $\tilde{T}^{n-1} = \hat{\rho}_c$, and $\tilde{f}^{n-1} = \hat{f}$, find $\tilde{c}$, $\tilde{T}$ and $\tilde{f}$ such that for all $\boldsymbol{x} \in \overline{\Omega} \setminus \Gamma_{\text{in}}$

$$\frac{d\tilde{c}}{dt} + H_{\text{gr}}^c = f_\ell^c \qquad \text{in } (t^{n-1}, t^n),$$

$$\frac{d\tilde{T}}{dt} + H_{\text{gr}}^T = f_\ell^T \qquad \text{in } (t^{n-1}, t^n), \qquad (14)$$

$$\frac{\partial \tilde{f}}{\partial t} + \frac{X}{UL} G \frac{\partial \tilde{f}}{\partial \ell} = \frac{X_\infty}{U_\infty f_\infty} (A_+ + A_-) \quad \text{in } (t^{n-1}, t^n) \times \Omega_\ell.$$

by considering the spatial variable $\boldsymbol{x}$ as a parameter. Note that the system of equations in (13) are decoupled. The concentration and the energy equations have to be solved once, whereas the PSD equation in (13) has to be solved for all $\ell \in \Omega_\ell$ by considering ℓ as a parameter. In the second step (14), two ordinary differential equations and a PSD equation in internal space (one-dimensional) have to be solved. Since the equations in (14) are coupled, an iteration of fixed point type is used to solve this system for all $\boldsymbol{x} \in \overline{\Omega} \setminus \Gamma_{\text{in}}$. To be consistent with the direct approach, only the first step of the fixed point iteration is applied. Nevertheless, the iterative procedure is not expensive as the iteration has to be applied between the one-dimensional PSD equation and two ordinary differential equations.

In the splitting scheme, the backward Euler method is used for the temporal discretization of the (12). Since the splitting scheme allows to use different spatial discretizations in Step 1 and Step 2, respectively, the standard Galerkin discretization is used for all scalar equations in (13), whereas the Ilin-Allen-Southwell finite difference scheme is used for the PSD equation in (14). Even though the Ilin-Allen-Southwell scheme is uniformly stable and second order consistent for an equation with fixed diffusion, the scheme shifts automatically to a simple first order upwind scheme for equations with zero diffusivity as in (14), see [25] for more details.

The transformation to an axisymmetric form will be presented exemplary for the equation for the concentration. It proceeds in the same way for the other equations. Before applying the axisymmetric transformation, the variational forms of the equations in (12) are derived and the boundary conditions are incorporated. Next, to obtain an axisymmetric form, volume and surface integrals in the variational forms have to be transformed into area and line integrals, respectively. Apart from the advantage of reducing one space dimension of the model equations, the derivation of the axisymmetric form from the variational formulation leads naturally to the boundary condition along the 'artificial rotational axis'. For details, it is referred to [8].

Let $\boldsymbol{u}(x, y, z) = (u_1, u_2, u_3)$ and $\boldsymbol{u}_c(r, z, \phi) = (u_r, u_\phi, u_z)$ be the representation of the velocity in the Cartesian and cylindrical coordinates, respectively. It will be assumed that the velocity is independent of ϕ and $u_\phi = 0$. The scalar quantities, pressure, mass of the solute, temperature, and PSD are also assumed to be independent of ϕ and they are denoted by $p = p(r, z)$, $c = c(t, r, z)$, $T = T(t, r, z)$, and $f = f(t, r, z, \ell)$, with

$$r(x, y) = \sqrt{x^2 + y^2} \quad \text{and} \quad \phi(x, y) = \arctan(y/x), \quad 0 \le \phi(x, y) < 2\pi.$$

Since finite element methods are used for discretizing the equation for the concentration one needs a variational formulation of this equation. To this end, considering the first equation of (12), multiplying it with a test function ψ, applying integration by parts, and incorporating the boundary condition yields

$$\int_\Omega \frac{\partial c}{\partial t}\, \psi \; d\boldsymbol{x} + \frac{1}{Pe_c} \int_\Omega \nabla c \cdot \nabla \psi \; d\boldsymbol{x} + \int_\Omega (\boldsymbol{u} \cdot \nabla)\, c\, \psi \; d\boldsymbol{x} + \int_\Omega H_{\text{gr}}^c\, \psi \; d\boldsymbol{x} = \int_\Omega f_\ell^c\, \psi \; d\boldsymbol{x}.$$

This equation can be rewritten in the following form, using the $L^2(\Omega)$ inner product $(\cdot, \cdot)_\Omega$,

$$\left(\frac{\partial c}{\partial t}, \psi \right)_\Omega + a_c\, (c, \psi) = f_c\, (\psi),$$

where $a_c\, (c, \psi)$ is a bilinear form and $f_c\, (\psi)$ is the source integral given by

$$a_c\, (c, \psi) := \frac{1}{Pe_c} \int_\Omega \nabla c \cdot \nabla \psi \; d\boldsymbol{x} + ((\boldsymbol{u} \cdot \nabla)\, c, \psi)_\Omega + \left(H_{\text{gr}}^c, \psi \right)_\Omega$$
$$f_c\, (\psi) := (f_\ell^c, \psi)_\Omega.$$

Now, the integrals have to be transformed to the two-dimensional domain Φ

spanned by (r, z). For the solute mass c and their test function ψ, one has

$$c(x, y, z) = c(r(x, y), z), \quad \frac{\partial c}{\partial x} = \frac{\partial c}{\partial r} \cos\phi, \quad \frac{\partial c}{\partial y} = \frac{\partial c}{\partial r} \sin\phi, \quad \frac{\partial c}{\partial z} = \frac{\partial c}{\partial z},$$

$$\psi(x, y, z) = \psi(r(x, y), z), \quad \frac{\partial \psi}{\partial x} = \frac{\partial \psi}{\partial r} \cos\phi, \quad \frac{\partial \psi}{\partial y} = \frac{\partial \psi}{\partial r} \sin\phi, \quad \frac{\partial \psi}{\partial z} = \frac{\partial \psi}{\partial z}.$$

Applying these relations, one obtains

$$\iiint_\Omega c\,\psi\,d\boldsymbol{x} = 2\pi \iint_\Phi c\,\psi\,r\,dr\,dz.$$

Next, the bilinear form $a_c(c, \psi)$ and the source integral become

$$a_c(c, \psi) = 2\pi \iint_\Phi \left[\frac{1}{Pe_c} \left(\frac{\partial c}{\partial r}\frac{\partial \psi}{\partial r} + \frac{\partial c}{\partial z}\frac{\partial \psi}{\partial z} \right) + \left(u_r \frac{\partial c}{\partial r} + u_z \frac{\partial c}{\partial r} + H_{\mathrm{gr}}^c \right) \psi \right] r\,dr\,dz,$$

$$f_c(\psi) = 2\pi \iint_\Phi f_\ell^c\,\psi\,r\,dr\,dz.$$

The symmetry condition at the (artificial) axial boundary, i.e., at $r = 0$, is given by

$$\left. \frac{\partial c}{\partial \boldsymbol{n}} \right|_{r=0} = 0,$$

which is a natural boundary condition. Note that, in comparison with the two-dimensional integrals in Cartesian coordinates, only an additional factor 'r' has to be used in the implementation of the axisymmetric form, whereas the factor 2π gets canceled on both sides of the equation.

In the direct discretization, the equation for the PSD is discretized with a finite difference method. The application of the axisymmetric approach could have only an impact on the last term on the left-hand side of (7). But since $u_2 = u_3 = u_\phi = u_z = 0$, it turns out that in the considered setup nothing changes in comparison with the formulation in Cartesian coordinates.

3.4   Computing the Aggregation

The difficulty in the computation of the aggregation term comes from the double integral in (9). To compute this integral accurately, special numerical methods have to be applied. The method used in the simulations presented below is described in [12,13]. This state-of-the-art method exploits the separable structure of the aggregation kernel and uses the FFT to solve the convolution integrals. The application of this method requires the use of special grids, which are piecewise equi-distant with respect to the volume of the particles. In the simulations, the grid is refined towards the smallest particles because there are much more small particles in the system than larger ones. To avoid
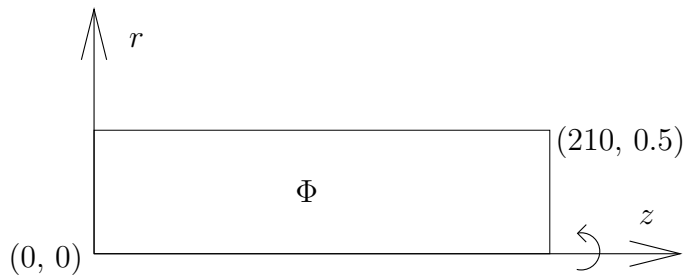
Fig. 1. Two-dimensional axisymmetric computational domain.

the decrease of mass, a correction to the aggregation term is computed as follows:

$$A(V) := A(V) - \text{mass}(A(V)) \frac{2}{V_{\max}^2 - V_{\min}^2}, \tag{15}$$

where $V_{\max}$, $V_{\min}$ are the smallest and largest volumes of the particles.

4 Numerical Studies

4.1 Setup of the Simulations

The non-dimensional flow domain is a cylindrical pipe of length 210 and radius 0.5. This domain is somewhat longer than the pipe in the experiments (200). The reason for extending the pipe was that boundary conditions at the outlet Γ_{out} are not known from the experiments. Possible differences between the actual boundary conditions and the boundary conditions presented in Section 2 should not influence the numerical results at $z = 200$, where the behavior of the PBS was monitored. This goal is achieved by choosing the computational domain a little bit longer than the actual domain. In the axisymmetric formulation, the computational domain is $\Phi = (0, 210) \times (0, 0.5)$, see Figure 1.

From the experiments, data at $z = 2$ m are known for two flow rates, namely $V_r = 30$ ml/min and $V_r = 90$ ml/min. These flow rates correspond to Hagen-Poiseuille profiles of the form

$$\boldsymbol{u} = U_{\text{in},\cdot} \left(\frac{1}{4} - r^2, 0 \right)$$

with $U_{\text{in},30} = 5.09296$ for 30 ml/min and $U_{\text{in},90} = 15.27887$ for 90 ml/min. Experimental data $f_{\text{seed}}(\ell)$ for the PSD at the inlet Γ_{in} are available. Their form and their conversion for utilizing them in numerical simulations is described in detail in [14, Section 4]. Following [14], the non-dimensional inlet condition

13

Table 1
Number of degrees of freedom (including Dirichlet nodes).

	coarse grid	fine grid
temperature	1521	5729
concentration	1521	5729
PSD	142974	538526

at $z = 0$ has the form

$$f_{\text{in}}(t, r, 0, \ell) = \frac{1}{f_\infty} \frac{6 \cdot 10^7}{300 \ V_r} f_{\text{seed}}(\ell), \quad t \in [0, 1000],$$

where $t_e = 1000$ is the final computation time. In contrast to the setup in [14], there is a continuous entering of particles into the domain and for both considered flow regimes one obtains finally a steady-state solution. This situation facilitates the assessment of the studied solvers.

The experimental reference data to compare with is the normalized time-space-averaged volume fraction q_3. The normalized volume fraction is defined by

$$q_3(t, r, z, \ell) = \frac{\ell^3 f(t, r, z, \ell)}{\int_{\ell_{\min}}^{\ell_{\max}} \ell^3 f(t, r, z, \ell) \ d\ell}.$$

At the final time $t_e = 1000$, where the steady state was reached, a spatial averaging of the PSD for $z = 200$ was performed, for each discrete particle diameter ℓ_i, $i = 1, \ldots 94$, and then the volume fraction was computed as a function of the diameter. Finally, the normalization was applied.

Equidistant time steps of length $\tau = 0.01$ were used in the computations. The domain Φ was triangulated with uniform grids (equidistant in each direction) consisting of rectangles. On the coarser grid 168×8 rectangles were used and on the finer grid 336×16 rectangles. On both grids, Q_1 finite elements were applied. For the grid with respect to the internal coordinate, the same grid as in [14] was applied. It satisfies the requirements for applying the FFT for computing the aggregation terms and it has 94 nodes. The corresponding numbers of degrees of freedom for the two grids are presented in Table 1.

All simulations were performed with the research code MOONMD [16].

For completing the model of the PBS, the parameters in the aggregation kernel have to be found. They were determined by calibrating the numerical results for the normalized space-averaged volume fraction with the experimental data. For $U_{\text{in},30}$, a good calibration of the curve could be obtained with $C_{\text{sh}} = 8.5 \cdot 10^{-5}$ and $C_{\text{br}} = 7 \cdot 10^3$, see Figure 2. In the other case $U_{\text{in},90}$, the values which were found to be appropriate are $C_{\text{sh}} = 7 \cdot 10^{-5}$ and $C_{\text{br}} = 7 \cdot 10^3$. This value for C_{sh} is slightly smaller than in the case $U_{\text{in},30}$. A decrease of this value for

14

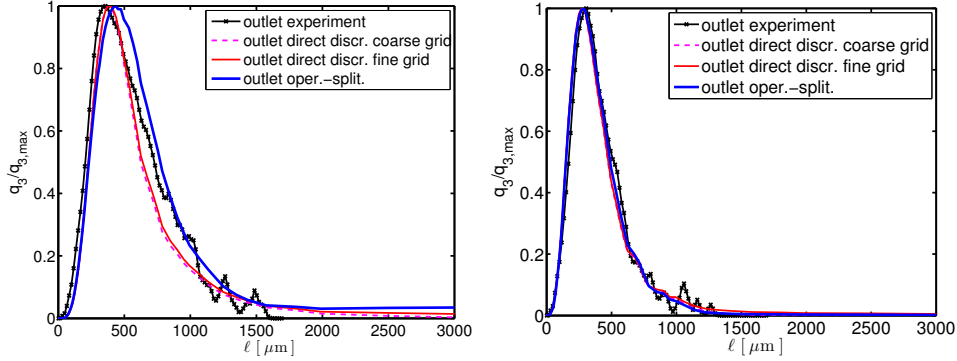faster flows was also observed in [14], but the difference is smaller in the setup considered here.

Fig. 2. Normalized space-averaged volume fraction at the outlet with optimal aggregation parameters for both solvers, left for $U_{in,30}$, right for $U_{in,90}$.

Comparing the values of C_{sh} and C_{br} with those of [14], one can observe that in the present setup both values are smaller by almost two orders of magnitude. This means that the aggregation has less influence on the behavior of the PSD and consequently that the growth of particles has a much stronger impact to fit the reference curves, compared with the setup considered in [14]. This difference in the behavior can be explained with the different ways the concentration and the particles are injected into the flow domain in both setups. In [14], the injection is performed only in the center of the inlet plane. Following mainly the flow direction, there is little influence of the walls in this setup. In the model considered here, both concentration and particles are injected uniformly at the complete inlet plane. The cool wall lead to a relatively small saturation concentration, see (1), such that the growth rate (2) becomes large. Since also a lot of particles are near the wall, the growth of particles is stimulated. In addition, particles near the wall have a much longer residence time (in which they can continue to grow) than particles in the center of the channel. Altogether, growth is a much more important mechanism in the considered setup than in [14].

4.2 Computational Results

The curves for the normalized space-averaged volume fraction at the outlet in the steady state are shown in Figure 2. It can be observed that both solvers give almost indistinguishable results for $U_{in,90}$. In case of the lower velocity $U_{in,30}$, the curve of the operator-splitting scheme is shifted somewhat to the right. That means, this scheme predicts a higher amount of larger particles than the direct discretization. In our opinion, the explanation for this behavior comes from the different orders of the numerical schemes for computing the growth of the particles. The direct discretization uses a third order scheme,

whereas a first order method, which is considerably more diffusive, is used in the operator-splitting scheme. This numerical diffusion leads to a smearing of the results and hence to the prediction of a higher amount of larger particles. A similar observation was made in [20]. It shall be emphasized that in the case of the fast flow, and with that of a short residence time of the particles, no impact of the numerical diffusion on the normalized space-averaged volume fraction is visible.

Having a detailed look on individual points at the outlet, Figure 3, one can see that the results between the two solvers for $U_{\text{in},30}$ differ considerably in the center of the channel and that they are similar away from the center. From the curve at the center it can be clearly seen that the operator-splitting scheme predicts larger particles. For the case $U_{\text{in},90}$, the presentation of curves for the individual points is omitted for the sake of brevity. Like for the space-averaged curves in Figure 2, there are almost no differences in the curves for the individual points.
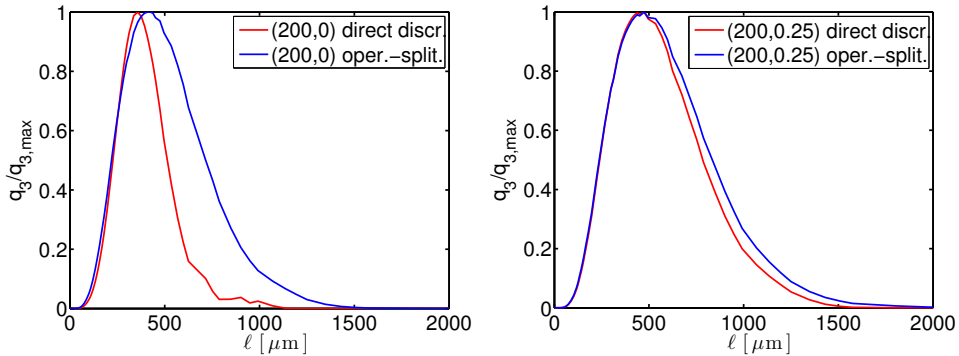

Fig. 3. Normalized space-averaged volume fraction at different points at the outlet for $U_{\text{in},30}$, fine grid.

Considering the PSD at the center of the outlet, Figure 4, one can see clearly the smearing effect of the first order scheme used in the operator-splitting scheme. The peak of the corresponding curve is somewhat smaller than for the direct discretization and there are more larger particles with $\ell \geq 500$ μm, which have a notable impact on the volume fraction. It can be also observed that the direct discretization predicts more particles from nucleation.

In Figure 5, the PSD in different points at the outlet for the direct discretization is presented. It can be seen that there is a notable amount of larger particles also away from the center, which is in contrast to the results from [14, Figure 8] and which supports the explanation concerning the greater importance of the growth in the present setup.

The convergence to the steady state is illustrated with the evolution of the mean temperature, the mean concentration, and the mean PSD, see Figures 6
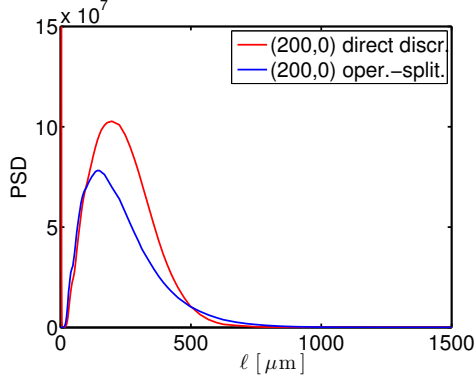
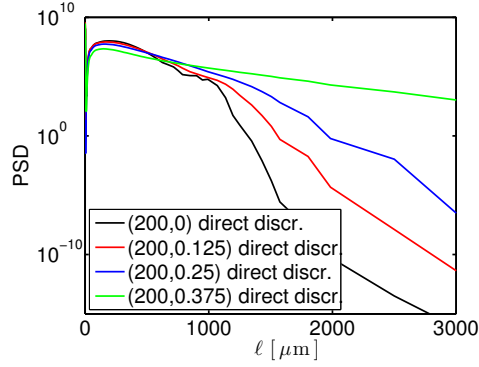Fig. 4. PSD in the center of the outlet for $U_{in,30}$, fine grid.

Fig. 5. PSD in different points at the outlet for $U_{in,30}$ and the direct discretization, fine grid.

– 8. The mean values are given by

$$\frac{\int_\Phi Tr\ drdz}{\int_\Phi r\ drdz}, \quad \frac{\int_\Phi cr\ drdz}{\int_\Phi r\ drdz}, \quad \frac{\int_{\ell_{min}}^{\ell_{max}} \int_\Phi fr\ drdzd\ell}{\int_{\ell_{min}}^{\ell_{max}} \int_\Phi r\ drdzd\ell}.$$

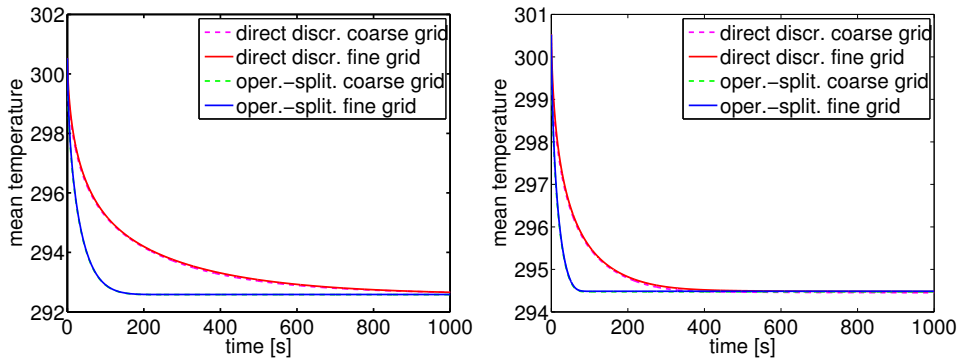Fig. 6. Temporal evolution of the mean temperature for both solvers, left $U_{in,30}$, right $U_{in,90}$.

It can be observed that the simulations with the operator-splitting scheme attain the steady state much faster than the simulations with the direct dis-
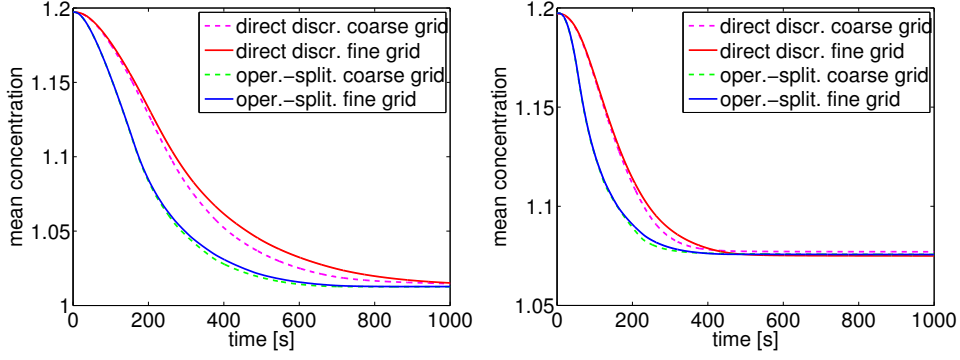
17

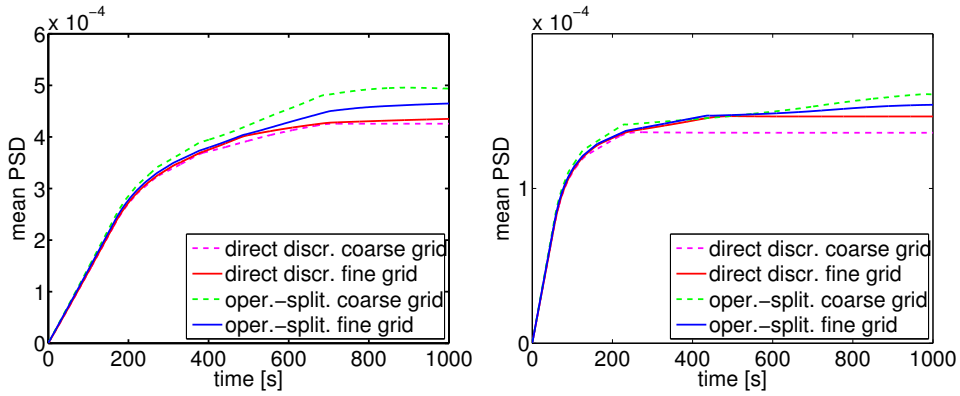Fig. 7. Temporal evolution of the mean concentration for both solvers, left $U_{\text{in},30}$, right $U_{\text{in},90}$.

Fig. 8. Temporal evolution of the mean PSD for both solvers, left $U_{\text{in},30}$, right $U_{\text{in},90}$.

cretization. At the final time, the results are similar. The largest difference can be observed for the mean PSD. Probably, the main reason is again the different order of the schemes used for computing the growth. The fineness of the grid has only a slight impact for both solvers. is used. The differences of the mean PSD between both schemes are smaller on the finer grid, i.e., a grid convergence can be already observed. Since the direct discretization applies a higher order scheme, it can be expected that the evolution of the mean values is predicted by this scheme more accurately than with the operator-splitting scheme. A better accuracy of higher order schemes for solving PBSs has been observed also in [20]. The numerical diffusion contained in the operator-splitting scheme leads right from the beginning of the simulation to relatively large particles, which consume immediately a lot of energy and concentration for continuing to grow. Thus, the mean values for temperature and concentration decrease faster than for the direct discretization and the mean value for the PSD increases faster.

Table 2
Average computing time per time step.

	direct discretization				operator-splitting			
	Step 1	aggr.	Step 2	total	Step 1	aggr.	Step 2	total
coarse grid	0.05	1.43	0.20	1.68	0.036	1.43	0.17	1.64
fine grid	0.20	5.88	0.84	6.92	0.156	5.92	0.67	6.73

4.3   Efficiency

In the direct discretization scheme, the solution of the PBS is computed in two steps, see Section 3.1. The linear system of equations obtained form the discretization of solute and energy equations are solved with the sparse direct solver UMFPACK [5]. After having computed the aggregation term, the solution of the PSD equation is obtained with an explicit scheme. Hence, the solution of a large system of algebraic equations is not necessary in the direct discretization.

The solution of the PBS with the operator-splitting scheme also consists two steps, see Section 3.2. Since the coupled terms including the growth rate are handled in the second step of the operator-splitting scheme, the system matrices of the scalar equations in the first step (13) do not change in time. Therefore, the system matrices are assembled and factorized (LU) once at the first time step, and the same LU factorization is used in the sparse direct solver UMFPACK in the subsequent time steps. In the second splitting step (14), the system of algebraic equations are solved also with UMFPACK.

All simulations are performed using a HP SL390s computer with 3467 MHz Xeon processors and 96 GB RAM. The average computing times taken by the direct discretization and by the operator-splitting scheme for one time step are presented in the Table 2. For both schemes and on both grids, the computation of the aggregation is very expensive, around 85 % to 90 % of the total computing time. Further, it has to be noted that the average computing time per time step increases four times when the grid is uniformly refined. Excluding the computing time of the aggregation, the time taken by the two solvers are comparable, with the operator splitting scheme being a little bit faster. On the one hand, this scheme gains efficiency by avoiding the solution of a problem in a higher-dimensional domain. But on the other hand, the application of an explicit scheme for the PSD equation in the direct discretization turned out to be also quite efficient. Overall, the computing times are dominated by the times needed for computing the aggregation. Hence, the improvement of the efficiency of the aggregation step is the key for improving the overall performance of both solvers.

19

The main results and conclusions from the numerical studies are summarized below.

- Both solvers led to qualitatively the same results in the steady state, with small quantitative differences. The differences were larger for the situation that the particles have a long residence time in the flow domain.
- Considerable differences could be observed between the schemes in the prediction of the transition from the initial to the steady state.
- The operator-splitting scheme attained the steady state with much less time steps. Thus, if one is interested only in the steady state, this approach should be preferred.
- Because of the use of a higher order method in the direct discretization, it is expected that the direct discretization predicts the evolution from the initial to the steady state more accurately. Thus, if one is interested in the evolution of the process, the application of this scheme is recommended.
- The overall computing times for both solvers and on both grids were dominated by the time for computing the aggregation.
- Excluding the time needed for computing the aggregation, both solvers were similarly efficient, with the operator-splitting scheme being a little bit faster in our implementation.

5   Outlook

We will pursue two main directions of research in the near future. First, moment-based methods will be incorporated into the systematic numerical studies. And second, more complex models will be considered. In these models, the simulation of the flow field might be necessary, the solution of the PBS will not converge to a steady state, and, certainly most important, the PSD will be multi-variate.

From the results presented in this paper one can conclude that the low order discretization of (14) in the operator-splitting scheme should be replaced by a higher order method if the evolution of the PSD is studied. For increasing the efficiency, above all the computation of the aggregation term needs to be performed faster. Since this computation in each spatial node is independent of the computation in the other nodes, some sort of parallelization can be done in a straightforward way and will be certainly very helpful.

References

[1] N. Ahmed, G. Matthies, and L. Tobiska. Stabilized finite element discretization applied to an operator-splitting method of population balance equations. *Appl. Numer. Math.*, 70:58–79, 2013.

[2] N. Ahmed, G. Matthies, L. Tobiska, and H. Xie. Finite element methods of an operator splitting applied to population balance equations. *J. Comp. Appl. Math.*, 236:1604–1621, 2011.

[3] C. Borchert and K. Sundmacher. Crystal aggregation in a flow tube: Image-based observation. *Chemical Engineering & Technology*, 34(4):545–556, 2011.

[4] Róbert Bordás, Volker John, Ellen Schmeyer, and Dominique Thévenin. Numerical methods for the simulation of a coalescence-driven droplet size distribution. *Theor. Comput. Fluid Dyn.*, 27(3-4):253–271, 2013.

[5] Timothy A. Davis. Algorithm 832: UMFPACK V4.3—an unsymmetric-pattern multifrontal method. *ACM Trans. Math. Software*, 30(2):196–199, 2004.

[6] S. Ganesan. An operator-splitting heterogeneous finite element method for population balance equations: Stability and convergence. Preprint 1531, WIAS, Berlin, 2010.

[7] S. Ganesan. An operator-splitting Galerkin/SUPG finite element method for population balance equations: Stability and convergence. *ESAIM: M2AN*, 46:1447–1465, 2012.

[8] S. Ganesan and L. Tobiska. An accurate finite element scheme with moving meshes for computing 3D-axisymmetric interface flows. *Int. J. Numer. Methods Fluids*, 57(2):119–138, 2008.

[9] S. Ganesan and L. Tobiska. Implementation of an operator-splitting finite element method for high-dimensional parabolic problems. Preprint 04–11, Otto-von-Guericke-Universität Magdeburg, Fakultät für Mathematik, 2011.

[10] S. Ganesan and L. Tobiska. An operator-splitting finite element method for the efficient parallel solution of multidimensional population balance systems. *Chem. Eng. Sci.*, 69(1):59–68, 2012.

[11] S. Ganesan and L. Tobiska. Operator-splitting finite element algorithms for computations of high-dimensional parabolic problems. *Appl. Math. Comp.*, 219:6182–6196, 2013.

[12] W. Hackbusch. On the efficient evaluation of coalescence integrals in population balance models. *Computing*, 78:145 – 159, 2006.

[13] W. Hackbusch. Approximation of coalescence integrals in population balance models with local mass conservation. *Numer. Math.*, 106:627 – 657, 2007.

[14] Wolfgang Hackbusch, Volker John, Aram Khachatryan, and Carina Suciu. A numerical method for the simulation of an aggregation-driven population balance system. *Internat. J. Numer. Methods Fluids*, 69(10):1646–1660, 2012.

[15] V. John, I. Angelov, A.A. Öncül, and D. Thévenin. Techniques for the reconstruction of a distribution from a finite number of its moments. *Chem. Eng. Sci.*, 62(11):2890 – 2904, 2007.

[16] Volker John and Gunar Matthies. MooNMD—a program package based on mapped finite element methods. *Comput. Vis. Sci.*, 6(2-3):163–169, 2004.

[17] Volker John, Teodora Mitkova, Michael Roland, Kai Sundmacher, Lutz Tobiska, and Andreas Voigt. Simulations of population balance systems with one internal coordinate using finite element methods. *Chem. Eng. Sci.*, 64(4):733 – 741, 2009.

[18] Volker John and Julia Novo. On (essentially) non-oscillatory discretizations of evolutionary convection-diffusion equations. *J. Comput. Phys.*, 231(4):1570–1586, 2012.

[19] Volker John and Michael Roland. On the impact of the scheme for solving the higher dimensional equation in coupled population balance systems. *Internat. J. Numer. Methods Engrg.*, 82(11):1450–1474, 2010.

[20] Volker John and Carina Suciu. Direct discretizations of bi-variate population balance systems with finite difference schemes of different order. *Chem. Eng. Sci.*, 106(0):39 – 52, 2014.

[21] M. Krasnyk, M. Mangold, S. Ganesan, and L. Tobiska. Numerical reduction of a crystallizer model with internal and external coordinates by proper orthogonal decomposition. *Chem. Eng. Sci.*, 70:77–86, 2012.

[22] Dmitri Kuzmin. Explicit and implicit FEM-FCT algorithms with flux linearization. *J. Comput. Phys.*, 228(7):2517–2534, 2009.

[23] Daniele L. Marchisio and Rodney O. Fox. Solution of population balance equations using the direct quadrature method of moments. *Journal of Aerosol Science*, 36(1):43 – 73, 2005.

[24] Robert McGraw. Description of aerosol dynamics by the quadrature method of moments. *Aerosol Science and Technology*, 27(2):255–265, 1997.

[25] H.-G. Roos, M. Stynes, and L. Tobiska. *Numerical Methods for Singularly Perturbed Differential Equations.* Springer-Verlag, 2008.

[26] M.V. Smoluchowski. Versuch einer mathematischen Theorie der Koagulationskinetik kolloider Lösungen. *Z. Phys. Chem.*, 92:129 – 168, 1917.